Transient Dynamics of a Porous Sphere in a Linear Fluid

P. Cano Fossi[1], P. Nourian[2], R. Khare[2], and S. Bhattacharya[1†]

[1]*Department of Mechanical Engineering, Texas Tech University, Lubbock, TX, 79409, USA*
[2]*Department of Chemical Engineering, Texas Tech University, Lubbock, TX, 79409, USA*

†*Corresponding Author Email: s.bhattacharya@ttu.edu*

ABSTRACT

This article describes the unsteady translational motion of a porous sphere with slip-surface in a quiescent viscous fluid. Apart from its radius a and density ρ_s, the particle is characterized by its permeability parameter γ, slip-length l and effective viscosity-ratio ϵ for interior flow. The Reynolds number for the system is assumed to be small leading to negligible convective contribution, though the transient inertia for both the liquid and the solid is comparable to viscous forces. The resulting linearized but unsteady flow-equations for both inside and outside the porous domain are solved in time-invariant frequency domain by satisfying appropriate boundary conditions. The analysis ultimately renders frequency-dependent hydrodynamic friction for the suspended body. The frictional coefficient is computed under both low and high frequency limit for different values of γ, l and ϵ so that the findings can be compared to known results with impermeable surface. Moreover, the parametric exploration shows that the sphere acts like a no-slip body even with non-zero l if $a\gamma \gg \frac{1}{\sqrt{\epsilon}}$. Scaling arguments from a novel boundary layer theory for flow inside porous media near interfaces explain this rather unexpected observation. Also, computed fluid resistance is incorporated in equation of motion for the particle to determine its time-dependent velocity response to a force impulse. This transient response shows wide variability with ρ_s, γ, l and ϵ insinuating the significance of the presented study. Consequently, the paper concludes that slip and permeability should be viewed as crucial features of submicron particles if unexpected variability is to be explained in nano-scale phenomena like nano-fluidic heat conduction or viral transmission. Thus, the theory and findings in this paper will be immensely useful in modeling of nano-particle dynamics.

1. INTRODUCTION

Microscale particles with complex structures are ubiquitous in nature. An important kind among them consists of either a porous body or a porous shell around a solid core. In this article, the main objective is to describe the time-dependent translational motion of such permeable microscopic solid particles inside a viscous fluid. Accordingly, we present a general formulation to analyze these unsteady dynamics assuming linearized flow-equations under low Reynolds number condition.

The transport of the porous species is of great importance in many practical contexts such as reaction engineering, electrochemical separations, water treatment, and medicine. Typically, these applications stem from the situations where Brownian mechanics of permeable solids are important, as our theory can be coupled with Green-Kubo relation to find particulate diffusivity. There are three specific contemporary technological necessities where our analysis would have direct relevance because the Brownian motion described by our theory plays a key role in all these systems.

Firstly, the motion of polyelectrolyte molecules or flocs of ions plays an important role in analysis or separation applications (Wei & Keh, 2004; Huang & Keh, 2015; Tsai & Lee, 2019) This diffusiophoretic motion of particulate aggregates through a fluid medium takes place in response to a concentration gradient or an electrical field and can be modeled as the translation of porous particles through a fluid medium. Another similar mechanism in different contexts can be seen in waste-water treatment. In that case, the simulated motion of porous particles could serve as a model system, where the settling velocity of waste matter coagulates is an important

parameter in designing sedimentation basins (Vahedi & Gorczyca, 2012).

The second application involves fixed bed reactors n the chemical processing industry. These systems involve a cylindrical reactor that is packed with porous catalyst particles. The reaction mixture flows through the packed bed and the reaction of interest takes place on the catalyst surface, where existing pores can greatly increase the surface area that is available for the reaction. The physicochemical processes in the system consist of fluid flow over the catalyst particles and through the pores. Moreover, the system behavior is dictated by reaction and diffusion of species, as well as any associated heat transfer taking place due to the resulting heat generation (Dixon, 2010; Solsvik & Jakobsen, 2011). An understanding of the fluid mechanics of the process will help simplify the modeling effort involved in designing such applications.

Thirdly and finally, biological entities like pollen grains are naturally occurring porous particles. Furthermore, some of the viruses with dense external spiked protein can be modeled as a submicron body with an outer porous layer. An understanding of the motion of such harmful particulate matters through the nasal cavity followed by the respiratory mucus is crucially needed in the field of medicine. This is essential for designing treatments for diseases that affect human airways, such as asthma (Fahy & Dickey, 2010; Schuster, 2013). The use of pollen grains as carriers for drug delivery is also being explored (Mundargi et al. 2016) – material transport processes are crucial in designing these applications.

Apart from the aforementioned technological applications, the Brownian and transport dynamics of porous particles plays considerable roles in various cutting-edge scientific explorations. For example, this mechanics can provide explanation behind strange behavior of nano-fluids where addition of a trace amount of submicron solutes causes disproportional increase in thermal conductivity (Chen, 2001; Eastman et al., 2001; Kincaid & Cohen, 2002). Often, this unexpected phenomenon is attributed to DLVO (Derjaguin-Landau-Verwey-Overbeek) theory assuming clustering networks formed by the nano-particles (Marconnet et al., 2013). Surprisingly, the anomalous enhancement of the thermal properties can also be seen for non-agglomerating species, especially if these have porous complex structures indicating the crucial impact of particulate permeability. Such phenomenon can be attributed to Brownian motion where the suspended solutes act as numerous spontaneous stirrer. Moreover, in recent years, advent of the bead microrheology technique (Mason & Weitz, 1995) has led to a renewed interest in the motion of microscale particles in complex media. Techniques of microrheology have been used in both experiments (Furst & Squires, 2017) and simulations (Karim et al. 2012; Nourian et al. 2021; Karim et al. 2016) to determine the rheology of soft matter. These techniques rely on quantitative relationships between the steady and unsteady motion of the particles and the viscoelastic properties of the media in which the particle motion takes place. Such relationships are available for the motion of the solid (i.e., non-porous) particles both in the presence and absence of slip at the particle surface (Karim

et al. 2012; Mason, 2000; Premlata & Wei, 2019). Extension of these ideas to understand the motion of porous particles such as pollen grains in soft matter necessitates quantitative relationships between motion of porous macro-molecules and the medium viscoelastic properties.

To this end, although steady dynamics of a porous body has been the primary focus in the literature, a few studies have considered unsteady flow past permeable bodies (Looker & Carnie, 2004; Vainshtein & Shapiro, 2009; Prakash & Raja Sekhar, 2012). However, there is a lack of thorough understanding of the interplay between the permeability and the degree of slip affecting the hydrodynamics mobility of a porous particle for different frequency of oscillation in an unsteady flow. In this study, our aim is to elucidate the combined effect of these factors. This means that the resulting theory would be the first analysis where surface slip and bulk permeability are considered together in description of an unsteady particulate motion in a viscous fluid.

The motion of an impermeable spherical particle through a quiescent viscous fluid is one of the most studied fluid mechanics problems (Navardi & Bhattacharya, 2013; Navardi et al., 2015) which is often referred to as Stokesian analysis. A related problem to this genre is the motion of a porous particle through a fluid medium (Yao et al., 2019). Flow through a porous medium is traditionally modeled using the semi-empirical Darcy's law which employs the medium permeability to provide a relationship between the fluid flow rate (or velocity) and the pressure drop. Darcy's law has been extensively used for quantifying flow through a packed bed of particles as is the case in filtration applications. On the other hand, use of the Brinkman equation is the preferred strategy for modeling flow through a porous particle (Higdon & Kojima, 1981; Masliyah, 1987; Yu & Kaloni, 1988; Keh & Chou, 2004; Keh & Lu, 2005; Prakash & Sekhar, 2017; Neale et al. 1973). In such a case, the flow inside the porous particle as represented using the Brinkman equation is coupled with the flow outside the particle that is modeled using the Stokes equation (for low Reynolds number applications). The two sets of equations are coupled via the boundary conditions involving continuity of the velocity and the stress components. Such considerations are the central tenet of our analysis presented in this paper.

Accordingly, this article is organized in the following way. In section 2, we outline the governing relations and boundary conditions for a translating porous sphere with slip-surface in viscous fluid. Section 3 converts the formulation in Fourier space by exploiting separable spatial and temporal derivatives so that the dynamics can be described in frequency domain replacing time dependence. The consequent temporally invariant but frequency dependent field solutions are derived in section 4. These solutions render frequency-dependent hydrodynamic friction for different values of system-defining parameters like permeability and slip-lengths in section 5. The corresponding time-dependent velocity response of the spherical particle to a force-impulse is
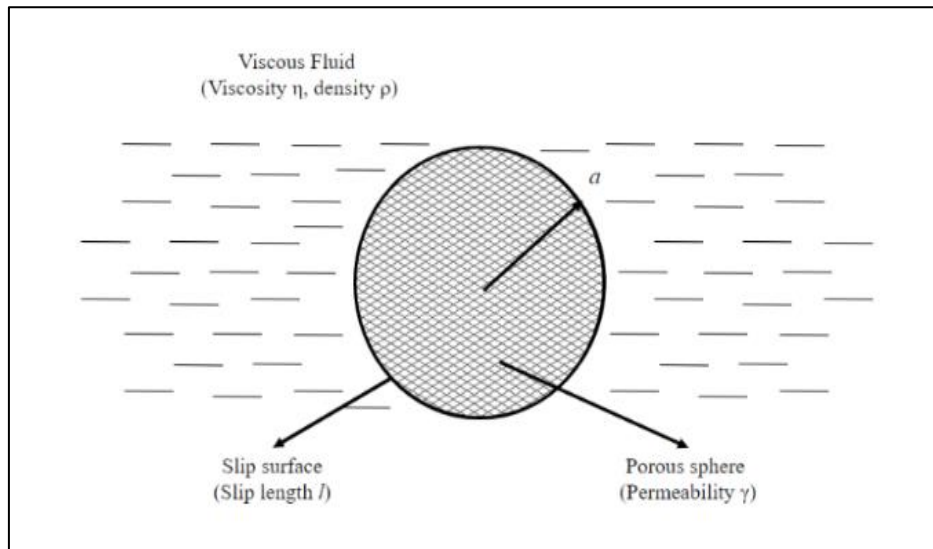
Fig. 1 Schematic of the porous particle translating within a viscous fluid

analyzed in section 6. Finally, the paper is summarized, and the conclusions are drawn in section 7.

2. DESCRIPTION OF THE SYSTEM

We consider a spherical porous particle of mass m and radius a translating in an unbounded Newtonian fluid of viscosity η and density ρ at a significantly low Reynolds number. The capillary number for the system is also very small ensuring insignificant effects of surface tension. The solid body experiences an external impulsive force $\boldsymbol{f}_{ext}$ which instigates its subsequent translation over time. The sphere is entirely filled with porous matter. Its porosity is represented by a permeability constant γ so that ηγ² represents the Darcy's proportionality constant between local velocity field and the additional induced stress exchanged across solid and liquid phase. The surface of the sphere is very smooth compared to the particulate dimension so that the fluid cannot have a purely no-slip condition at the interface. The resulting slip can be completely characterized by a length l which enters in a corresponding mixed boundary condition for velocity. Our primary goal in this study is to describe the time-dependent translation of the aforementioned particle in terms of friction coefficient and mobility response. The former is expressed in frequency space whereas the latter is calculated as a temporal function. To obtain these, we compute the velocity field inside and outside of the porous solid solving the corresponding flow equations with appropriate conditions for continuity at the solid-liquid interface. The schematic of the particle inside viscous fluid is shown in Fig.1. Though the present analysis is focused on a single sphere in unbounded space, the presented formalism can be extended in the future to cluster of spheres or ellipsoidal bodies in confined or unconfined liquid. The modified geometry can be accommodated by using different basis functions and their transformations as indicated in Navardi et al., 2015.

2.1 Equation of Motion for the Particle

The rectilinear motion of the moving particle over time is dependent on the applied forces according to

Newton's second law which can be written in the following form:

$$m\frac{d\boldsymbol{u}}{dt} = \boldsymbol{f}^{ex} + \boldsymbol{f}^{h} \tag{1}$$

Here, $\boldsymbol{u}$ represents the translational velocity of the porous body as it varies with time t. On the right hand side of the equation 1, $\mathbf{f}^{ex}$ and $\mathbf{f}^{h}$ stand for the applied external force and the hydrodynamic force exerted on the solid, respectively. In our study, we are specifically interested in Brownian dynamics of a porous sphere. Accordingly, the model considers the exerted external force to be impulsive in nature, as Brownian impacts are high-intensity short-duration instigations. This means that the temporal variation of the applied force is expressed in terms of Dirac delta function $\delta(t)$ so that:

$$\boldsymbol{f}^{ex} = \delta(t)\hat{\boldsymbol{e}} \tag{2}$$

Here, $\hat{\boldsymbol{e}}$ defines the direction in which the exerted force is applied. We consider a unidirectional problem with unique $\hat{\boldsymbol{e}}$. This, however, does not sacrifice any generality due to the linearity of the flow equations. As a result, our analysis can also describe a curvilinear trajectory by superposing the linear responses from all directions.

The hydrodynamic contribution in force $\boldsymbol{f}^{h}$ is computed from the solution of the velocity field. This force is given as a convolution:

$$\boldsymbol{f}^{h} = \int_{-\infty}^{t} \boldsymbol{F}^{h}(t - t') \cdot \boldsymbol{u}(t')dt' \tag{3}$$

where the effect of past motion on $\boldsymbol{f}^{h}$ in later time is taken into account. This is a well-known relation for flow-systems with memory due to transient inertia causing phase-lag between instigated motion and induced stress as long as the non-linear terms are negligible (Nourian et al. 2021). Hence, the friction tensor $\boldsymbol{F}^{h}$ depends on both the current time t and the past time t' so that it can represent the inertial memory of the system properly. In absence of the temporal inertia for steady systems, the time-dependence in $\mathbf{F}^{h}$ becomes a Dirac delta function with

stresses only impacted by instantaneous velocity. For our problem, this temporal variation has to be evaluated from unsteady hydrodynamic fields. Thus, our immediate goal is to find the flow inside and around the particle.

2.2 Inside and Outside Field Equations

Porosity of the particle allows the outside fluid to slip into the solid creating a velocity field inside the body. Thus, the system is governed by the flow dynamics between two distinct regions -- exterior and interior domains relative to the particle. The governing flow equations for both subdomains are considered separately.

For this purpose, we take a spherical coordinate system around the particulate center with radial distance from the origin denoted as r. For submicron Brownian species, the various scales for the motion are dictated by thermal fluctuations. The corresponding velocity scale is much smaller compared to $\eta/(\rho a)$ for micron-size particles. Thus, the non-linear convective inertia of the fluid becomes negligible relative to the viscous force making the momentum equation linear. On the other hand, the time-scale of the dynamics is dictated by the viscosity-induced decay in the system. As a result, the temporal acceleration of the fluid matches exactly with the dissipative contributions. This is why the unsteady version of the linearized Navier-Stokes equation is identified as the governing relation for our problem. Thus, the following relation for the external region with $r > a$ are considered in our model:

$$\rho \frac{\partial \boldsymbol{v}}{\partial t} = -\nabla p + \eta \nabla^2 \boldsymbol{v}. \tag{4}$$

Here, $\mathbf{v}$ and p represent the absolute velocity of the fluid and the hydrodynamic pressure outside the body,

For the internal region $r < a$, the system is described by Brinkman's unsteady model assuming the submicron solids to larger than 100nm so that continuum mechanics inside these remains valid. Accordingly, we consider:

$$\rho \frac{\partial \mathbf{v}_p}{\partial t} = -\nabla p_p + \epsilon \eta \nabla^2 \mathbf{v}_p - \gamma^2 \eta \mathbf{v}_p \tag{5}$$

where $\mathbf{v}_p$ and p_p represent the relative velocity field and the pressure inside the body, respectively. The constant γ denotes the permeability factor of the porous sphere while ϵ is the ratio between the effective viscosity of the fluid in the porous medium and its nominal value under unbounded condition. This is a standard model for flow in a porous medium simply imported from well-known literature (Premlata & Wei 2019). The characteristic Reynolds number for the flow through the permeable solid is even smaller than the same in the outside, as velocity reduces in the interior. Hence, for $r < a$ also, the convective inertia is negligible justifying the consideration of linearized governing equation.

For the internal flow, the velocity scale is even smaller than the one for the outside due to the additional resistance in the porous medium. At the same time, the temporal scale remains unaffected, as it is always dictated by the viscous decay. Thus, eq. 5 is also linearized unsteady momentum equation like eq. 4. It should be noted eq. 5 reduces to eq. 4 when both $\epsilon \rightarrow 1$ and $\gamma \rightarrow 0$.

The fluid is incompressible both inside and outside the solid leading to the following continuity equations:

$$\nabla \cdot \boldsymbol{v} = 0, \quad \text{and} \quad \nabla \cdot \boldsymbol{v}_p = 0 \tag{6}$$

These complete the sets of equations for both inner and outer flows, respectively.

2.3 Boundary Conditions

The equations for the exterior and interior of the porous body are to be solved in the presence of three sets of boundary conditions. Firstly, the outside flow far away from the particle has to vanish as the ambient fluid is quiescent. Secondly, the inner flow needs to be regular at the center of the sphere so that all unphysical singularities can be avoided. Thirdly and finally, appropriate continuity conditions for the velocity and the stress have to be satisfied at the solid-liquid interface. The continuity of the flow field at the solid-liquid interface is required to ensure no unphysical accumulation of fluid at that surface. This means that the normal relative velocity of the liquid with respect to the solid has to be exactly the same in the two region for $r = a$. Moreover, if the stress on the fluid-phase has to be finite, the tangential components of both relative velocities should also match. Thus, we conclude:

$$\boldsymbol{v}_p = \boldsymbol{v} - \boldsymbol{u} \tag{7}$$

where according to our earlier definition $\mathbf{v}_p$ is interpreted as relative to the solid body while $\boldsymbol{v}$ is an absolute velocity in an inertial reference frame. This is why the translation of the solid body must be subtracted from the $\boldsymbol{v}$ in the outer region in order to construct the condition.

Similarly, the continuity of stress at the solid-liquid interface is necessary so that no unbalanced force acts on it causing infinite acceleration. Consequently, equating the normal components of the traction vector along unit vector $\hat{\boldsymbol{n}}$ from two regions we find:

$$-p + \eta \hat{\boldsymbol{n}} \cdot [\nabla \boldsymbol{v} + (\nabla \boldsymbol{v})^T] \cdot \hat{\boldsymbol{n}} = -p_p + \epsilon \eta \hat{\boldsymbol{n}} \cdot \left[\nabla \boldsymbol{v}_p + \left(\nabla \boldsymbol{v}_p\right)^T\right] \cdot \hat{\boldsymbol{n}} \tag{8}$$

In contrast, the tangential components of the traction vector have an additional complexity due to the slip condition at the surface. The existence of slip implies that the interfacial shear stress on the outer fluid depends not only on the velocity gradients but also on the relative velocity itself. This renders the following mixed boundary condition involving identity tensor $\boldsymbol{I}$:

$$(\boldsymbol{I} - \hat{\boldsymbol{n}}\hat{\boldsymbol{n}}) \cdot (\boldsymbol{v} - \boldsymbol{u})$$
$$= l(\boldsymbol{I} - \hat{\boldsymbol{n}}\hat{\boldsymbol{n}}) \cdot \left[\nabla \boldsymbol{v} + (\nabla \boldsymbol{v})^T - \epsilon \left(\nabla \boldsymbol{v}_p + \left(\nabla \boldsymbol{v}_p\right)^T\right)\right] \cdot \hat{\boldsymbol{n}} \tag{9}$$

When the slip-length becomes 0, eq. 9 represents the usual no-slip condition making the solid and liquid velocity same at the boundary. With the introduction of slip, however, fluid no longer adheres to the surface necessitating introduction of a mixed condition like eq. 9 to describe continuity in shear force.

Under appropriate parametric values, the system of interfacial constraints represents an impermeable sphere. However, when slip, permeability and transiency are

simultaneously present in the dynamics, the limiting conditions for impermeability are non-trivial. One of our ultimate goals in the subsequent analysis will be to identify and explain these limits for which the solid appears as impermeable.

3. DECOMPOSITION IN FOURIER SPACE

The transport process under consideration is a slow-moving but fast-decaying phenomenon which allows linearization of the governing equations 4 and 5 earlier by neglecting the non-linear convective acceleration. This also implies that the temporal and material derivatives of all variables are approximately equal permitting replacement of the latter by the former in the entire formulation. Thus, the temporal dependence in the system of equations enters only due to $\partial/\partial t$ which renders a complete set of functional representation by its eigen functions $\exp(i\omega t)$. Consequently, the governing relations can be cast into a time-invariant form if the variables are transformed into frequency space ω using the Fourier function $\exp(i\omega t)$. Accordingly, we consider Fourier transform of the particulate translation as well as all field variables. The corresponding transformations for the equation of motion and the equation of fields yield the desired time-invariant formulation where spatial coordinates remain the only independent variables. The resulting dependence on frequency ω appears only as a parametric variation. From physical perspective, different ω represents cumulative effect of different temporal dependence caused by all sinusoidal excitations. Its larger values are associated to fast change in short time, whereas its smaller values depict behavior at large time-scale.

3.1 Fourier Transform of a Particle In Motion

The frequency dependent transformation of the translational velocity of the particle is defined in the Fourier integral:

$$\boldsymbol{u}(t) = \int_{-\infty}^{\infty} \hat{\boldsymbol{u}}_\omega \, e^{i\omega t} d\omega \tag{10}$$

When eq. 10 is inserted in eq. 1, the Fourier transform of the equation of motion can be obtained:

$$i\omega m \hat{\boldsymbol{u}}_\omega = \boldsymbol{f}_\omega^{ex} + \boldsymbol{f}_\omega^{h} \tag{11}$$

Here, acceleration is transformed to $i\omega\hat{\boldsymbol{u}}_\omega$ due to properties of derivatives in a convolution. Also, $\boldsymbol{f}_\omega^{ex}$ and $\boldsymbol{f}_\omega^{h}$ are the external applied force and the hydrodynamic force in Fourier space, respectively.

The impulsive external force represented by temporal dependence $\delta(t)$ yields a simple Fourier transform:

$$\boldsymbol{f}_\omega^{ex} = \frac{1}{2\pi}\hat{\boldsymbol{e}} \tag{12}$$

In contrast, the convolution expressing hydrodynamic force in eq. 2.3 makes $\boldsymbol{f}_\omega^{h}$ product of two frequency-dependent quantities:

$$\boldsymbol{f}_\omega^{h} = \widehat{\boldsymbol{F}}_\omega^{h} \cdot \hat{\boldsymbol{u}}_\omega \tag{13}$$

where $\boldsymbol{F}_\omega^{h}$ is the friction tensor in Fourier space. The fluid and the porous sphere are isotropic as all properties have directional invariance implying $\widehat{\boldsymbol{F}}_\omega^{h} = F_\omega^h \boldsymbol{I}$. Consequently,

all three terms in eq. 11 are perfectly aligned with $\hat{\boldsymbol{e}}$ allowing the conversion of the vector relation to the following scalar one

$$\hat{u}_\omega = \frac{1}{2\pi} \frac{1}{i\omega m - \widehat{F_\omega^h}} \tag{14}$$

This describes the translational motion of the particle in Fourier space when $\hat{F}_\omega^h$ is known from the hydrodynamic analysis. Thus, our goal is to determine $\hat{F}_\omega^h$ as a function of ω by solving the time-invariant but frequency-dependent field equations.

3.2 Fourier Description of Field Solutions

The velocity and pressure fields outside the porous medium in Fourier space are expressed as:

$$\boldsymbol{v}(t,r) = \int_{-\infty}^{\infty} \widehat{\boldsymbol{v}}_\omega \, e^{i\omega t} d\omega \tag{15}$$

and

$$p(t,r) = \int_{-\infty}^{\infty} \hat{p}_\omega e^{i\omega t} d\omega \tag{16}$$

Here, $\widehat{\boldsymbol{v}}_\omega$ and $\hat{p}_\omega$ are the frequency-dependent velocity and pressure fields in the external region of the particle, respectively. Similarly, the time-invariant relative velocity and pressure field in the interior are given by:

$$\boldsymbol{v}_p(t,r) = \int_{-\infty}^{\infty} \widehat{\boldsymbol{v}}_{p\omega} \, e^{i\omega t} d\omega \tag{17}$$

and

$$p_p(t,r) = \int_{-\infty}^{\infty} \hat{p}_{p\omega} e^{i\omega t} d\omega \tag{18}$$

with $\widehat{\boldsymbol{v}}_{p\omega}$ and $\hat{p}_{p\omega}$ being the respective Fourier transforms.

The first time-invariant governing relation for $\widehat{\boldsymbol{v}}_\omega$ and $\hat{p}_\omega$ is derived by inserting equations 15 and 16 in eq. 4 implying:

$$i\omega\rho\widehat{\boldsymbol{v}}_\omega = -\nabla\hat{p}_\omega + \eta\nabla^2\widehat{\boldsymbol{v}}_\omega \tag{19}$$

The same process also renders analogous field equations for $\widehat{\boldsymbol{v}}_{p\omega}$ and $\hat{p}_{p\omega}$, when equations 17 and 18 are used in eq. 5:

$$i\omega\rho\widehat{\boldsymbol{v}}_{p\omega} = -\nabla\hat{p}_{p\omega} + \eta\left[\epsilon\nabla^2\widehat{\boldsymbol{v}}_{p\omega} - \gamma^2\widehat{\boldsymbol{v}}_{p\omega}\right] \tag{20}$$

These relations are complemented by the corresponding continuity conditions

$$\nabla \cdot \widehat{\boldsymbol{v}}_\omega = 0 \quad \text{and} \quad \nabla \cdot \widehat{\boldsymbol{v}}_{p\omega} = 0 \tag{21}$$

which are simply the Fourier transform of eq. 6.

The time-invariant formulation completes with proper Fourier transform of the boundary conditions as well. It is to be noted that all relations representing these boundary conditions are already in time-invariant form. Thus, equations 7, 8 and 9 are simply converted to:

$$\widehat{\boldsymbol{v}}_\omega - \hat{\boldsymbol{u}}_\omega = \widehat{\boldsymbol{v}}_{p\omega} \tag{22}$$

$$-\hat{p}_{\omega} + \eta \hat{\boldsymbol{n}}\hat{\boldsymbol{n}} : [\nabla \hat{\boldsymbol{v}}_{\omega} + (\nabla \hat{\boldsymbol{v}}_{\omega})^T]$$
$$= -\hat{p}_{p\omega}$$
$$+ \epsilon \eta \hat{\boldsymbol{n}}\hat{\boldsymbol{n}} : [\nabla \hat{\boldsymbol{v}}_{p\omega} + (\nabla \hat{\boldsymbol{v}}_{p\omega})^T] \qquad (23)$$

and

$$(I - \hat{\boldsymbol{n}}\hat{\boldsymbol{n}}) \cdot \hat{\boldsymbol{v}}_{p\omega} = l(I - \hat{\boldsymbol{n}}\hat{\boldsymbol{n}})$$
$$\cdot \Big[\nabla \hat{\boldsymbol{v}}_{\omega} + (\nabla \hat{\boldsymbol{v}}_{\omega})^T$$
$$- \epsilon \left(\nabla \hat{\boldsymbol{v}}_{p\omega} + (\nabla \hat{\boldsymbol{v}}_{p\omega})^T\right)\Big] \cdot \hat{\boldsymbol{n}} \qquad (24)$$

where all field variables are just replaced with their respective Fourier transforms.

4. TIME INVARIANT FIELD SOLUTIONS

This section describes the analytical solution of the velocity and pressure fields inside and outside the porous sphere generated by the exerted impulse. In our analysis, the general axi-symmetric solutions of the aforementioned fields in the respective regions are first determined in terms of unknown amplitudes. Then, these unknowns are evaluated from the algebraic relations produced by the boundary conditions.

4.1 General Solution of the External Region

The solutions for hydrodynamics fields involve two analytical steps. Firstly, we find the pressure in such a way that continuity equation is automatically satisfied. Then, the known pressure term is treated as a source in the momentum relation eq. 19 from which the expression of the velocity field is derived. Taking divergence of eq. 19 and considering solenoidal velocity, one can conclude that pressure has to be a harmonic function. Moreover, for the domain outside the sphere, $\hat{p}_{\omega}$ should decay far away from the solid body. Also, such a decaying harmonic field is defined by a single vector $\hat{\boldsymbol{e}}$, as it enters in the only inhomogeneous relation in the formulation when the external impulse is considered. When all the aforementioned features for $\hat{p}_{\omega}$ are taken into account, its solution can only be:

$$\hat{p}_{\omega} = -C_o \eta \lambda_{\omega}^2 a^2 \frac{\hat{\boldsymbol{e}} \cdot \boldsymbol{r}}{r^3} \qquad (25)$$

Here, the amplitude C_O is a constant and the frequency-dependent complex wave number $\lambda_{\omega} = \sqrt{\frac{i\omega\rho}{\eta}}$ is introduced to indicate the appropriate scale for the pressure.

The evaluated pressure field is then substituted in eq. 19 as a source term. Thus, the velocity is expressed as the sum of the corresponding particular integral and a homogeneous solution:

$$\hat{\boldsymbol{v}}_{\omega} = C_o \nabla \frac{\hat{\boldsymbol{e}} \cdot \boldsymbol{r}}{r^3} + C_o^H \Bigg[-\lambda_{\omega}^2 \frac{e^{-\lambda_{\omega}r}}{r} \hat{\boldsymbol{e}}$$
$$+ \nabla \left(\hat{\boldsymbol{e}} \cdot \nabla \frac{e^{-\lambda_{\omega}r}}{r}\right)\Bigg] \qquad (26)$$

where constant C_O^H represents the amplitude of the latter. The solution for $\hat{\boldsymbol{v}}_{\omega}$ has the appropriate decay at infinity congruent to the static fluid far away from the moving solid.

4.2 General Solution of the Internal Region

A similar approach is used to determine the hydrodynamic fields inside the porous medium. Like before, the governing equations ensure that pressure field $\hat{p}_{p\omega}$ must be a harmonic function which is a solution of Laplace equation. However, unlike the exterior domain, $\hat{p}_{p\omega}$ has to be regular without any singularity so that it remains finite at the origin. Finally, it has to be defined by a linear relation with the motion inducing force along $\hat{\boldsymbol{e}}$. All these criteria can only be satisfied if:

$$\hat{p}_{p\omega} = -C_p \epsilon \eta \lambda_{p\omega}^2 a^2 (\hat{\boldsymbol{e}} \cdot \boldsymbol{r}) \qquad (27)$$

where C_P is an unknown constant and $\lambda_{p\omega} = \sqrt{\frac{i\omega\rho}{\eta\epsilon} + \frac{\gamma^2}{\epsilon}}$ corresponds to a new complex wave-length modified by the impermeability factor γ^2 according to eq. 20. The inner and outer wave-numbers $\lambda_{p\omega}$ and λ_{ω} become exactly the same under the limit $\epsilon \to 1$ and $\gamma \to 0$.

When eq. 27 is used in the momentum relation for the porous medium, the velocity $\hat{\boldsymbol{v}}_{p\omega}$ is, like $\hat{\boldsymbol{v}}_{\omega}$, computed as the sum of the particular integral and the homogeneous solution:

$$\hat{\boldsymbol{v}}_{p\omega} = C_p \hat{\boldsymbol{u}}_{\omega} + C_p^H \Bigg[-\lambda_{p\omega}^2 \frac{\sinh(\lambda_{p\omega}r)}{r} \hat{\boldsymbol{e}}$$
$$+ \nabla \left(\hat{\boldsymbol{e}} \cdot \nabla \frac{\sinh(\lambda_{p\omega}r)}{r}\right)\Bigg] \qquad (28)$$

Here, the amplitude C_P^H is the constant associated to the homogeneous solution. It is to be noted that the regularity of $\hat{\boldsymbol{v}}_{p\omega}$ is satisfied by eq. 28 at the origin due to the property of sine hyperbolic function.

4.3 Coupling boundary conditions

The solutions for hydrodynamic fields inside and outside the porous medium can be coupled with the interfacial boundary conditions. This allows construction of a system of four algebraic relations corresponding to the continuity of velocity and stress-traction vectors across the solid-liquid interface in both normal and tangential directions. The four equations can be, then, used to find the four unknown amplitudes C_O, C_O^H, C_P, C_P^H whose evaluation provides the unique flow-solutions in both relevant domains.

Accordingly, we first focus on the interfacial continuity of velocity field by substituting equations 26 and 28 in eq. 22. The normal or radial component of the resulting equation yields:

$$\frac{C_o}{a^3} - \frac{C_o^H}{a^3}(\lambda_{\omega}^2 a^2 + \lambda_{\omega}a + 1)e^{-\lambda_{\omega}a} - C_p$$
$$+ \frac{C_p^H}{a^3}\big[(\lambda_{p\omega}^2 a^2 + 1)\sinh(\lambda_{p\omega}a)$$
$$- \lambda_{p\omega}a\cosh(\lambda_{p\omega}a)\big] = 1 \qquad (29)$$

A second relation from the vector boundary condition could have been obtained by its resolution along tangent of the surface. We, however, noticed a substantial simplification if the vectorial components are considered normal to $\hat{\boldsymbol{e}}$ instead. The consequent scalar relation involving such components is:

$$-3C_o + C_o^H(\lambda_\omega^2 a^2 + 3\lambda_\omega a + 3)e^{-\lambda_\omega a}$$
$$+ C_p^H\big[3\lambda_{p\omega}a\cosh(\lambda_{p\omega}a)$$
$$- (3 + \lambda_{p\omega}^2 a^2)\sinh(\lambda_{p\omega}a)\big] = 0 \quad (30)$$

Though equations 29 and 30 are obtained by decomposing components along two non-orthogonal directions, their linear independence is still assured by the proper spanning of the longitudinal plane. Next, the third relation is determined as

$$\frac{C_o}{a^3}\eta(\lambda_\omega^2 a^2 + 12) - \frac{C_o^H}{a^3}\eta(4\lambda_\omega^2 a^2 + 12\lambda_\omega a + 12)e^{-\lambda_\omega a}$$
$$- C_p\eta\epsilon\lambda_{p\omega}^2 a^2$$
$$+ \frac{C_p^H}{a^3}\eta\epsilon\big[(4\lambda_{p\omega}^2 a^2 + 12)\sinh(\lambda_{p\omega}a)$$
$$- 12\lambda_{p\omega}a\cosh(\lambda_{p\omega}a)\big] = 0 \quad (31)$$

by substituting the hydrodynamic field solutions into eq. 23 describing continuity of normal stress: Finally, the slip-stress at the solid-liquid interface is considered by coupling equations 24, 26 and 28 to derive the last relation:

$$\frac{C_o}{a^3}6l\eta - \frac{C_o^H}{a^3}l\eta(\lambda_\omega^3 a^3 + 3\lambda_\omega^2 a^2 + 6\lambda_\omega a + 6)e^{-\lambda_\omega a} + C_p$$
$$+ \frac{C_p^H}{a^3}\big[\lambda_{p\omega}a\cosh(\lambda_{p\omega}a)$$
$$- (\lambda_{p\omega}^2 a^2 + 1)\sinh(\lambda_{p\omega}a)$$
$$+ l\eta\epsilon\big[(3\lambda_{p\omega}^2 a^2 + 6)\sinh(\lambda_{p\omega}a)$$
$$- (\lambda_{p\omega}^3 a^3 + 6\lambda_{p\omega}a)\cosh(\lambda_{p\omega}a)\big]\big]$$
$$= 0 \quad (32)$$

We exploit equations 29 through 32 in a matrix form to compute C_O, C_O^H, C_P, C_P^H.

5. FREQUENCY-DEPENDENT HYDRODYNAMIC FRICTION

This section presents the variation of translational friction as a function of frequency for different values of l, γ and ϵ. For concise description of the parametric space, we normalize relevant quantities in nondimensional form by recognizing their respective scales. Accordingly, the subsequent calculations and results are all furnished in terms of appropriate dimension-less parameters and variables.

5.1 Non-Dimensional Matrix Formulation

The system of linear equations in 29 – 32 involving C_O, C_O^H, C_P, C_P^H is solved in a non-dimensional matrix form. For this purpose, we define the following dimension-less column of coefficients:

$$|c\rangle = \begin{bmatrix} C_O/a^3 \\ C_O^H/a^3 \\ C_P \\ C_P^H/a^3 \end{bmatrix} \quad (33)$$

where their respective dimensional scales are factored out.

The column of coefficients are coupled to interfacial conditions by the following matrix relation derived from equations 29 through 32:

$$[R]|c\rangle = |b\rangle \quad (34)$$

where the right-hand side is represented by

$$|b\rangle = \begin{bmatrix} 1 \\ 0 \\ 0 \\ 0 \end{bmatrix} \quad (35)$$

The square matrix [R] is 4 x 4 with terms dependent on frequency as well as system-defining parameters:

$$[R]$$
$$= \begin{bmatrix} 1 & f_1(\bar\omega)e^{-\overline{\lambda_\omega}} & -1 & g_1(\bar\omega) + h_1(\bar\omega) \\ -3 & f_2(\bar\omega)e^{-\overline{\lambda_\omega}} & 0 & g_2(\bar\omega) + h_2(\bar\omega) \\ \overline{\lambda_\omega}^2 + 12 & f_3(\bar\omega)e^{-\overline{\lambda_\omega}} & \epsilon\overline{\lambda_{P\omega}}^2 & \epsilon[g_3(\bar\omega) + h_3(\bar\omega)] \\ 6\bar{l} & f_4(\bar\omega)e^{-\overline{\lambda_\omega}} & 1 & g_4(\bar\omega) + h_4(\bar\omega) \end{bmatrix}$$
$$(36)$$

where $\bar{l}$ represents the non-dimensional slip which is defined as $\bar{l} = l/a$. We construct each of the four rows of the matrix [R] by identifying the coefficients attached to the elements of $|b\rangle$ in eqs.29—32, respectively. In other word, each of these four equations represents one row in [R]. Consequently, the matrix includes the following set of functions:

$$f_1(\bar\omega) = -(\overline{\lambda_\omega^2} + \overline{\lambda_\omega} + 1) \quad (37)$$

$$f_2(\bar\omega) = \bar\lambda_\omega^2 + 3\bar\lambda_\omega + 3 \quad (38)$$

$$f_3(\bar\omega) = 4\bar\lambda_\omega^2 + 12\bar\lambda_\omega + 12 \quad (39)$$

$$f_4(\bar\omega) = \bar{l}(\bar\lambda_\omega^3 + 3\bar\lambda_\omega^2 + 6\bar\lambda_\omega + 6) \quad (40)$$

$$g_1(\bar\omega) = (\bar\lambda_{p\omega}^2 + 1)\sinh(\bar\lambda_{p\omega}) \quad (41)$$

$$g_2(\bar\omega) = -(\bar\lambda_{p\omega}^2 + 3)\sinh(\bar\lambda_{p\omega}) \quad (42)$$

$$g_3(\omega) = (4\bar\lambda_{p\omega}^2 + 12)\sinh(\bar\lambda_{p\omega}) \quad (43)$$

$$g_4(\bar\omega) = -\big[\bar\lambda_{p\omega}^2 + 1 - 3\bar{l}\epsilon(\bar\lambda_{p\omega}^2 + 6)\big]\sinh(\bar\lambda_{p\omega}) \quad (44)$$

$$h_1(\bar\omega) = -\bar\lambda_{p\omega}\cosh(\bar\lambda_{p\omega}) \quad (45)$$

$$h_2(\bar\omega) = 3\bar\lambda_{p\omega}\cosh(\bar\lambda_{p\omega}) \quad (46)$$

$$h_3(\omega) = -12\bar\lambda_{p\omega}\cosh(\bar\lambda_{p\omega}) \quad (47)$$

$$h_4(\bar\omega) = \big[1 - \bar{l}\epsilon(\bar\lambda_{p\omega}^2 + 6)\big]\bar\lambda_{p\omega}\cosh(\bar\lambda_{p\omega}) \quad (48)$$

The first of these functions described in eqs.37-40 are all polynomials of $\bar\lambda_\omega = \lambda_\omega a$, which is the non-dimensional counterpart of λ_ω. In contrast, the last sets of relations 41 through 48 involve polynomic functions of dimension-less $\bar\lambda_{p\omega} = \lambda_{p\omega}a$. As both $\bar\lambda_\omega$ and $\bar\lambda_{p\omega}$ depend on the non-dimensional frequency $\bar\omega = \omega\eta/(\rho a^2)$, the matrix elements in eq. 36 are interpreted as functions of $\bar\omega$.

We refer to [R] as the frequency-dependent grand resistance matrix for our problem as $|c\rangle$ represents amplitudes for velocity, and the non-zero component of $|b\rangle$ appears for force impulse. We invert the grand resistance matrix and contract it with a row associated to induced
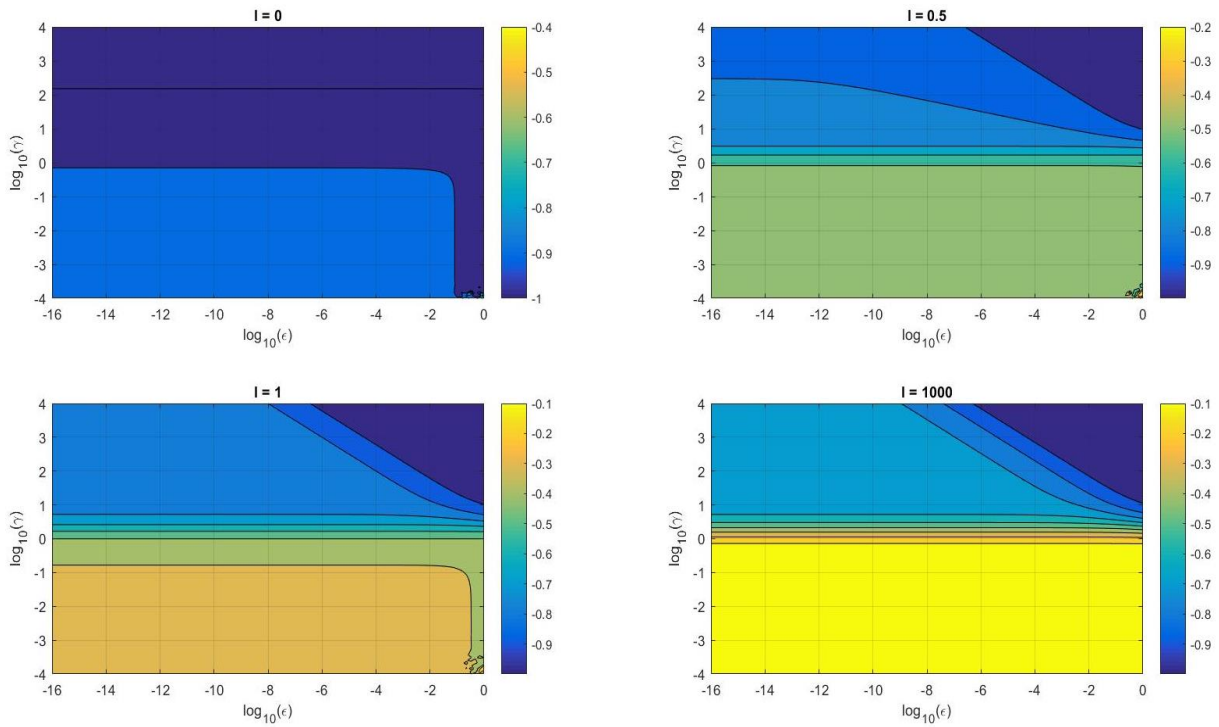
Fig. 2 Frequency-dependent friction normalized by Stokesian value for no-slip impermeable sphere plotted as a function of $\bar{\gamma}$ and ϵ under limit $\omega \to 0$ for $\bar{l} = 0$ (top left), $\bar{l} = 0.5$ (top right), $\bar{l} = 1$ (bottom left) and $\bar{l} = 1000$ (bottom right)

stress in order to compute the nondimensional hydrodynamic friction tensor given by:

$$\hat{\bar{F}}_\omega^H = \frac{\widehat{F_\omega^h}}{6\pi\eta a} = \frac{1}{6\pi}\langle f|R^{(-1)}|b\rangle \tag{49}$$

Here, components in row $\langle f|$ include the contribution in the hydrodynamic force exerted by the fluid on the surface of the particle due to the fields associated to C_O, C_O^H, C_P, C_P^H. The regularity of the solutions inside the porous medium ensures the last two contributions to be zero. The respective forces due to the outside flow are determined by integrating the stress tensor over the surface of the particle. A subsequent calculation with the application of the divergence theorem yields the following result:

$$\langle f| = \left\{ \frac{4\pi}{3}\bar{\lambda}_\omega^2 \quad \frac{8\pi}{3}\bar{\lambda}_\omega^2(\bar{\lambda}_\omega + 1) \quad 0 \quad 0 \right\} \tag{50}$$

The evaluation of $\hat{\bar{F}}_\omega^H$ using equations 35, 36, 49 and 50 completes the description of the hydrodynamic term in eq. 14 so that the translational motion of the porous sphere can be determined in Fourier space

5.2 Parametric Phase Diagram for Friction in Stokesian Limit

For weakly inertial cases under low-frequency limit, Stokesian analysis provides the hydrodynamic friction for an impermeable sphere with arbitrary slip. A few recent works (Premlata & Wei 2019) have expanded these findings for similar particles towards inertial regime by considering non-zero frequency. Thus, it is imperative that the limiting parametric conditions for impermeability are identified to distinguish between porous and non-porous

bodies. Then, we will be able to validate some of our calculations under limiting circumstances by comparing our data with previously known results. Moreover, such studies will reveal the underlying physics causing the observed parametric variations with system-defining quantities like, $\bar{\gamma} = \gamma a$, $\bar{l}$ and ϵ. Thus, phase-plots for hydrodynamic resistance in the space defined by the aforementioned three non-dimensional numbers are created to understand where the computed values coincide with the known ones.

In this subsection, the focus is the Stokesian regime with negligible frequency, whereas the inertial systems will be explored later. Accordingly, we set $\bar{\omega} \to 0$ to calculate $\hat{\bar{F}}_\omega^H$ using eq. 49 and present its phase-diagram with $\bar{\gamma}$, $\bar{l}$ and ϵ in Fig. 2. We consider four different values of $\bar{l}$ or four subplots there. Among these, $\bar{l} = 0$ means no-slip condition at the outer surface of the solid sphere, as the disappearing slip-length indicates exact matching of solid and liquid velocities at the interface. In contrast, very high $\bar{l}$ like $\bar{l} = 1000$ represents conditions for perfect slip where interfacial shear stress vanishes. The two other intermediate values (0.5 and 1) correspond to transitional cases in between the two aforementioned extremes. In each subplot, $\bar{\gamma}$ and ϵ are varied across several orders of magnitude to span the exploration window adequately. This is why these quantities are presented in terms of their logarithmic variations.

For $\bar{l} = 0$, the phase diagram is simple: when $\bar{\gamma} > 1$, the computation of normalized friction matches perfectly with the known value for no-slip impermeable spheres, as it approaches a value of -1. The results have insignificant variation with ϵ as long as its value is sufficiently smaller

than 1 which is always true in modeling of porous medium.

The plots, in contrast, become more complicated for non-zero values of $\bar{l}$. These phase diagrams indicate three distinct regimes separated by two consistent lines. First of these lines are rather intuitive — as for $\bar{l} = 0$, sufficiently large $\bar{\gamma}$ demarcates between permeable and impermeable spheres. Interestingly, a second line corresponding to $\bar{\gamma}\sqrt{\epsilon} \gg 1$ also appears unexpectedly in the picture differentiating two additional regimes with slip and no-slip, though both appear as non-porous solid. This obviously does not happen when $\bar{l} = 0$, as it always produces no-slip results by assigning the slip-length as 0. However, as soon as a non-zero slip-length is considered, the additional distinction with slip and no-slip remains evident at the exact location for the non-porous particles irrespective of the value of $\bar{l}$. We explain this coupling phenomenon between slip and penetration in the subsequent subsection by a novel boundary-layer theory.

5.3 Boundary Layer Explanation for the Coupling Between Impermeability and Slip

From Fig. 2, it is evident that the conditions for impermeability and slip to recover Stokesian results are not straight forward to define. Thus, we perform a scaling analysis based on the governing equations and interfacial boundary conditions in order to properly understand the impermeability and slip regimes for our analysis.

We first look into the velocity scales at the interior of the porous solid. The particular integral in eq. 28 implies that the only effect of the pressure gradient on this internal velocity field is to create a uniform potential flow irrespective of frequency. The corresponding potential flow is:

$$v_p^{pot} = \frac{\nabla p}{\eta\gamma^2} \tag{51}$$

where ∇p is the pressure gradient dictated by the external fields. Furthermore, under the low frequency limit, the viscous term for the outer flow is matched with ∇p in the governing equation 19 yielding such a pressure scale that

$$\nabla p \sim \eta U / a^2 \tag{52}$$

Here, U is the charadteristic velocity scale for the dynamics fixed by the initial translation of the particle. By combining equations 51 and 52, we find that the scale for the internal transport and the particulate translation are connected by the following relation:

$$v_p^{pot} \sim U / \overline{\gamma^2} \tag{53}$$

For an impermeable sphere, the potential flow inside it must be negligible compared to its translation. Thus, one can conclude the intuitive inference:

$$\bar{\gamma}^2 \gg 1 \tag{54}$$

as the condition for impermeability at low frequencies.

Interfacial conditions are mainly enforced by the homogeneous solutions in equations 26 and 28 where the flow in the porous body varies sharply inside a boundary-layer. Thus, if interfacial slip has to be accounted for, one should consider the residual velocity after subtracting the pressure-driven potential flow inside the solid. This makes the flow in the interior boundary layer purely shear-driven. Accordingly, unlike in classical boundary layer theory, the external pressure gradient does not affect the tangential slip velocity at the solid-liquid interface.

The scale for the interfacial shear stress responsible for the internal boundary layer can be obtained from equations 20 and 24. For this purpose, we first evaluate the characteristic boundary-layer thickness Δ by equating the viscous contribution with the Darcy's term $\gamma^2\eta v_p$ from equation 5:

$$\Delta = \frac{\sqrt{\epsilon}}{\gamma} \tag{55}$$

Then, the shear stress from the solid side can be determined by dividing the characteristic slip-velocity v_s by either l or Δ. This stress, however, has to match with the corresponding outer value U/a due to the external flow. Hence, we conclude that the slip velocity should be governed by the following scaling law:

$$\frac{U}{a} \sim \max\left(\frac{v_s}{l}, \frac{\epsilon v_s}{\Delta}\right) \implies v_s$$
$$= \min\left(\frac{U}{\sqrt{\epsilon}\bar{\gamma}}, \bar{l}U\right) \tag{56}$$

The dimensional analysis provides a striking inference — the slip velocity can be negligible compared to U under two separate circumstances. Firstly, if l is small compared to a, v_s obviously disappears. The second condition is the unexpected one — when $\sqrt{\epsilon}\bar{\gamma}$ is large, then also v_s/U becomes small even if l is way larger than a. The phase-diagrams with non-zero l in Fig. 3 simply demonstrate the second condition by exhibiting the additional demarcation line for $\sqrt{\epsilon}\bar{\gamma} \gg 1$ between partial-slip and no-slip systems.

Figure 3 conclusively establishes the presented boundary-layer argument and the derived scaling law. There, the tangential velocity is plotted as a function of radius around the interface at $r = l$. It clearly shows the formation of boundary-layer inside the solid. It is evident that its thickness is independent on l. The plots also reveal the non-obvious parametric variations in slip velocity. Firstly, it is exactly zero for all ϵ and $\bar{\gamma}$ if $\bar{l} = 0$. Then, it only varies with $\bar{l}$ when $\sqrt{\epsilon}\bar{\gamma} < 1$, but becomes invariant of $\bar{l}$ when $\sqrt{\epsilon}\bar{\gamma} \gg 1$. This is precisely what the boundary layer theory predicts and the phase-diagrams in Fig.2 indicate. Table 1 further summarizes all the aforementioned implications for all possible ranges of $\sqrt{\epsilon}\bar{\gamma}$ and slip length.

5.4 Parametric Phase Diagram for Inertial Limit

Next, we investigate the parametric phase-diagram for hydrodynamic friction $\hat{\bar{F}}_\omega^H$ under the inertial regime with large value of $\bar{\omega}$. For non-zero frequencies, $\hat{\bar{F}}_\omega^H$ is a complex number, as the effect of temporal acceleration causes a phase lag between the translational velocity and the hydrodynamic force. Accordingly, we present both the real and the imaginary parts of the quantity in Figs. 4 and 5, respectively.
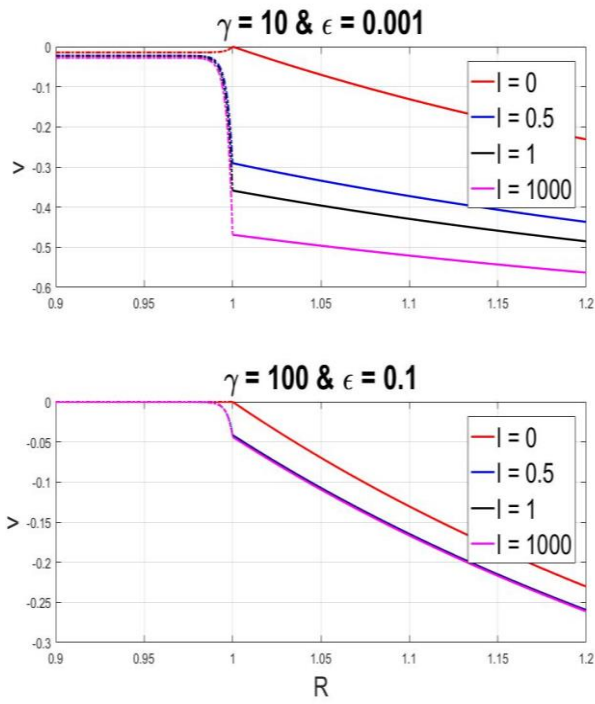
Fig. 3: Tangential relative velocity between solid and liquid at the spherical interface for different slip-lengths as a function of radial distance under Stokesian limit $\omega \to 0$ for $\sqrt{\epsilon}\bar{\gamma} \ll 1$ (top) and $\sqrt{\epsilon}\bar{\gamma} \gg 1$ (bottom)

Table 1 Summary of slip velocity v_s respect to non-dimensional conditions based of parametric values

	$\bar{l} \gg 1$	$\bar{l} \sim 0$	$\bar{l} \ll 1$
$\sqrt{\epsilon}\bar{\gamma} \gg 1$	$U/\sqrt{\epsilon}\bar{\gamma}$	$U/\sqrt{\epsilon}\bar{\gamma}$	$\bar{l}U$
$\sqrt{\epsilon}\bar{\gamma} \sim 1$	$U/\sqrt{\epsilon}\bar{\gamma}$	$U/\sqrt{\epsilon}\bar{\gamma}$ or $\bar{l}U$	$\bar{l}U$
$\sqrt{\epsilon}\bar{\gamma} \ll 1$	$\bar{l}U$	$\bar{l}U$	$\bar{l}U$

In Figs. 4 and 5, $\bar{\omega}$ is considered as 10^4 while other parameters are kept exactly same as in corresponding subplots of Fig.1. For such a high value of frequency, the imaginary part of the friction is supposed to be much larger than its real part. This is evident from Figs. 4 and 5. Interestingly, different domains in the phase-diagram for inertial regime mimic the ones seen for the Stokesian plots. As a result, we see only two regions corresponding to permeable and impermeable spheres for $\bar{l} = 0$ as before in subsection 5.2. Similarly, the appearance of a third subdomain in the impermeable region demarcating no-slip and partial-slip is also evident. Thus, we conclude that the essential dynamics inside the boundary-layer remains the same between the inertial and the Stokesian systems.

The inertial and Stokesian phase-diagrams differ in two details. Firstly, the real part has a non-monotonic variation with $\bar{\gamma}$ in contrast to either its imaginary counter part or the Stokesian friction. It is to be noted, however, that the real part of friction is subdominant for high frequency.
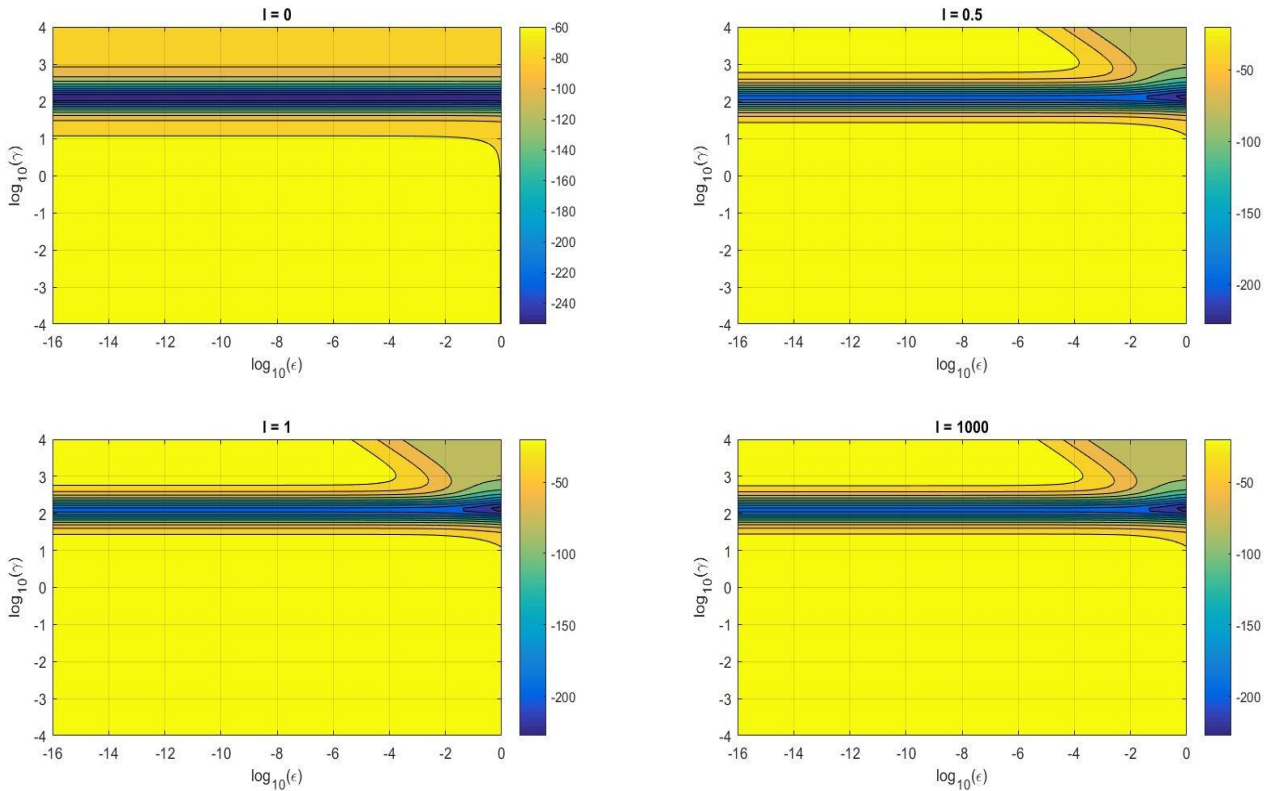

Fig. 4 Frequency-dependent real part of normalized hydrodynamic friction at $\bar{\omega} = 10^4$ plotted as a function of $\bar{\gamma}$ and ϵ for $\bar{l} = 0$ (top left), $\bar{l} = 0.5$ (top right), $\bar{l} = 1$ (bottom left) and $\bar{l} = 1000$ (bottom right)
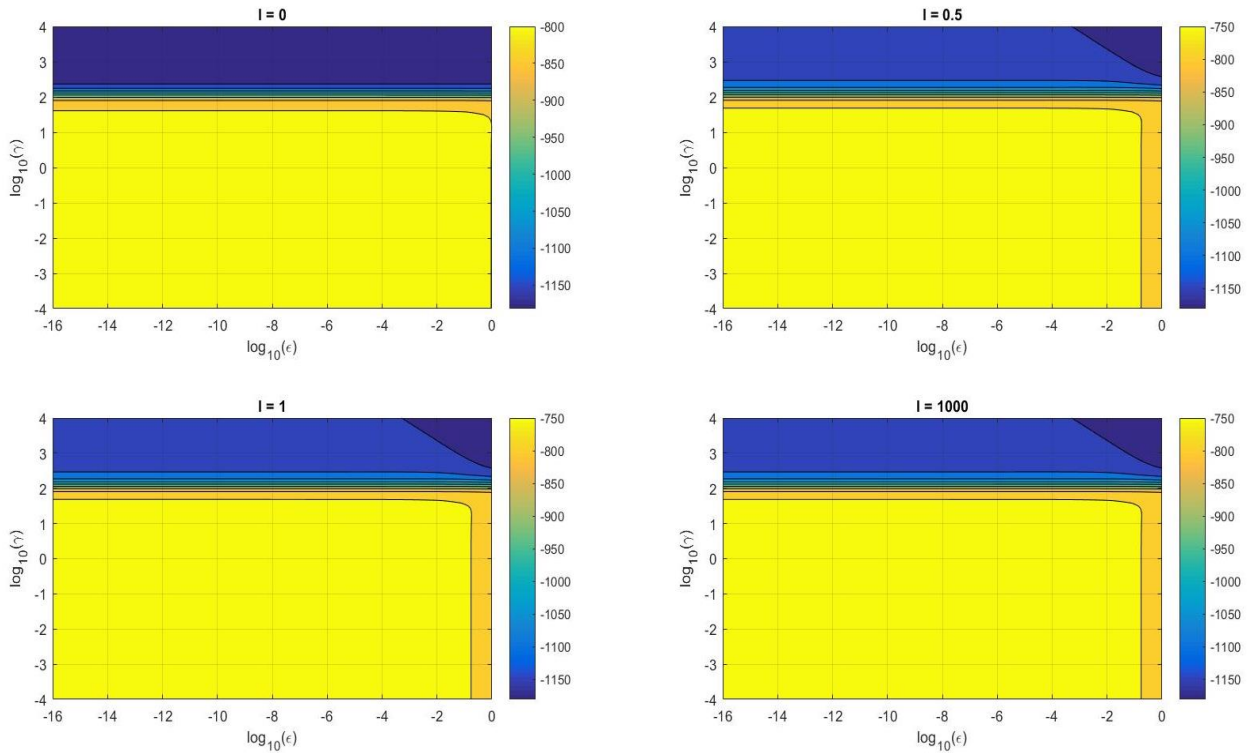
Fig. 5 Frequency-dependent imaginary part of normalized hydrodynamic friction at $\bar{\omega} = 10^4$ is plotted as a function of $\bar{\gamma}$ and ϵ for $\bar{l} = 0$ (top left), $\bar{l} = 0.5$ (top right), $\bar{l} = 1$ (bottom left) and $\bar{l} = 1000$ (bottom right)

As a result, it manifests several higher order effects which are really negligible contributions. In contrast, the second deviation from Stokesian plots involves predominant imaginary parts. It seems that the transition from permeable to impermeable regime happens for higher $\bar{\gamma}$. We see that for high frequencies this change appears only when

$$\overline{\gamma^2} \gg \bar{\omega} \qquad (57)$$

The reason behind this alteration is the fact that if eq. 57 is not satisfied, there will be short wave-length spatial fluctuations even inside the interior boundary-layer. Such oscillating fluid-flux affects the friction with modifications that cannot be seen in impermeable solids.

5.5 Spectra of Frequency Dependent Friction

Once different subdomains in the phase-diagram for the hydrodynamic friction are identified, it can be evaluated as a function of frequency for cases representing relevant parametric regimes. Accordingly, we present the spectral dependence of $\hat{\bar{F}}_\omega^H$ in Fig. 6 while choosing the values of system-defining parameters carefully. We consider three values of $\bar{l}$ corresponding to no-slip ($\bar{l} = 0$), partial slip ($\bar{l} = 0.5$) and full slip ($\bar{l} = 1000$) conditions. Then, $\bar{\gamma}$ and ϵ are selected in such a way that both permeable and impermeable particles as well as transition between the two are well described. We, however, do not venture to plot the case where no-slip condition can be reproduced by manipulating $\bar{\gamma}$ and ϵ even with non-zero $\bar{l}$, simply because the corresponding curve would look exactly as the one with $\bar{l} = 0$. Thus, to show all relevant spectral characteristics concisely, we kept ϵ

fixed at 10^{-10} and select three $\bar{\gamma}$ spanning the entire transitions from porous to non-porous sphere.

The plots in Fig.6 present both the real and imaginary parts of the friction. All these curves saturate quickly to their high-frequency asymptotic behavior dictated by the added mass of the accelerating fluid. The added mass creates the slope for the imaginary part of the friction as $\bar{\omega} \to \infty$. It also dictates the specific constant value at which the real part approaches at high frequency. We consider the range of $\bar{\omega}$ until 10 to make sure that the asymptotic behavior does not overwhelm the plots. All curves start from their expected Stokesian values which are non-zero for real $\hat{\bar{F}}_\omega^H$ and zero for the imaginary counterparts. It is evident from Fig. 6 that an impermeable sphere faces more resistance compared to a permeable one. This can be explained intuitively by noting that the latter provides additional path for the fluid to travel compared to the former just like a solid piston develops more pressure resistance than a leaky one. Curves for non-porous, partially porous and substantially porous spheres are sequentially placed. The last two merge with each other when frequency is adequately large due to the high-frequency low-wavelength fluctuations inside the interior boundary layer as discussed in the previous subsection.

In Fig. 7, we describe the nondimensional added mass as functions of $\bar{l}$ and $\bar{\gamma}$ by calculating the slope of the imaginary $\hat{\bar{F}}_\omega^H$ at $\bar{\omega} \to \infty$. We do not exhibit any dependence with ϵ in Fig. 7 because it has a very insignificant effect which cannot be displayed properly in the presence of other variations. Also, it is evident from Fig.7 that added mass alters significantly due to permeability effect only when $\bar{\gamma}$ varies from 100 to 10000,
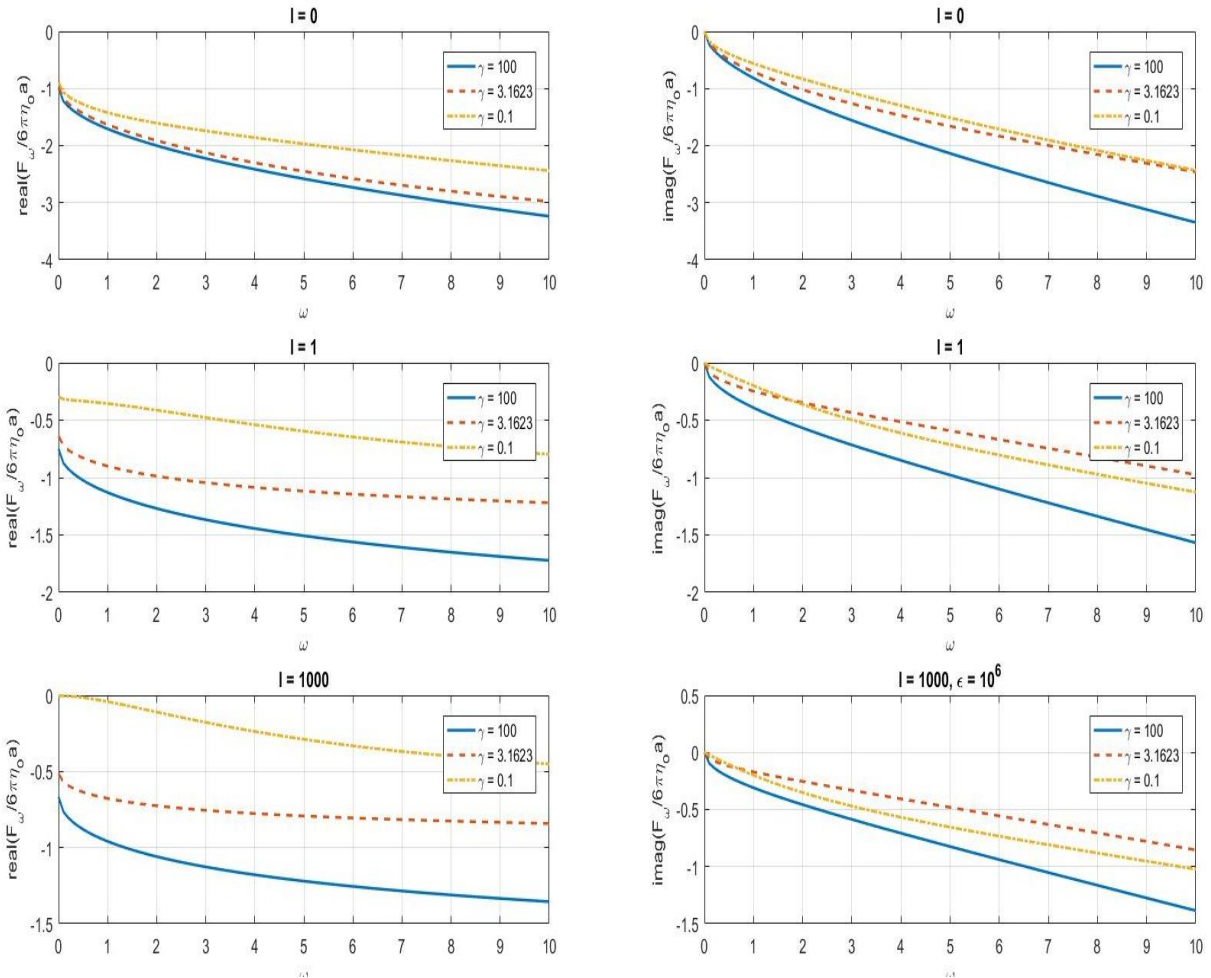
Fig. 6 Real and imaginary components of normalized hydrodynamic friction as a function of frequency for impermeable (blue), transitional (orange) and permeable (yellow) sphere with $\bar{l} = 0$ (top row), $\bar{l} = 1$ (middle row) and $\bar{l} = 1000$ (bottom row)
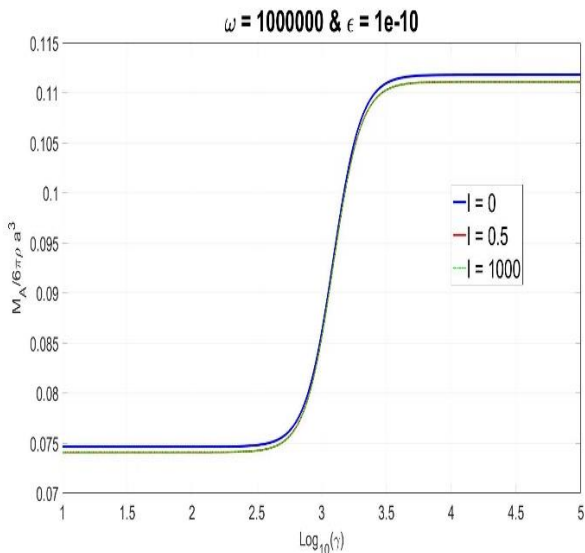

Fig. 7 Added mass as a function of $\bar{\gamma}$ for no-slip (blue), partial slip (red) and full slip (green) conditions

if $\bar{\omega} = 10^6$. This observed transition from permeable to impermeable sphere is consistent with the inequality given by eq. 57. It is well known from classical flow analysis

that dimension-less added mass is 1/9 for impermeable no-slip spheres when normalized by $6\pi\rho a^3$. Our simulation replicates this number for $\bar{l} = 0$ and $\bar{\gamma} \gg 1$. Moreover, the computed results match exactly with the recently published paper on the dynamics of impermeable particles for arbitrary $\bar{l}$ when $\bar{\gamma} \gg 1$ (Premlata & Wei 2019). This emphatically confirms the correctness of our analysis.

6. TIME-DEPENDENT MOBILITY RESPONSE FOR POROUS SPHERES WITH SLIP-SURFACES

In this section, we use the calculated $\hat{\bar{F}}_\omega^H$ to evaluate the temporally dependent mobility response defined by the velocity of the particle produced by the instantaneous impulse in later times. The requisite details of the computation along with mobility versus time plots for distinguishable parametric regimes are presented here. Moreover, we investigate the short duration impact of the impulse and compare it with the expected behavior for further verification of our analysis. These results are calculated for different $\bar{\gamma}$, $\bar{l}$ and ϵ as well as for solid-to-fluid density-ratio. In absence of fluid inertia, the resulting time-dependent curves correspond to exponential decays. However, when the flow equation includes transient acceleration, these velocity-responses would be non-trivial.
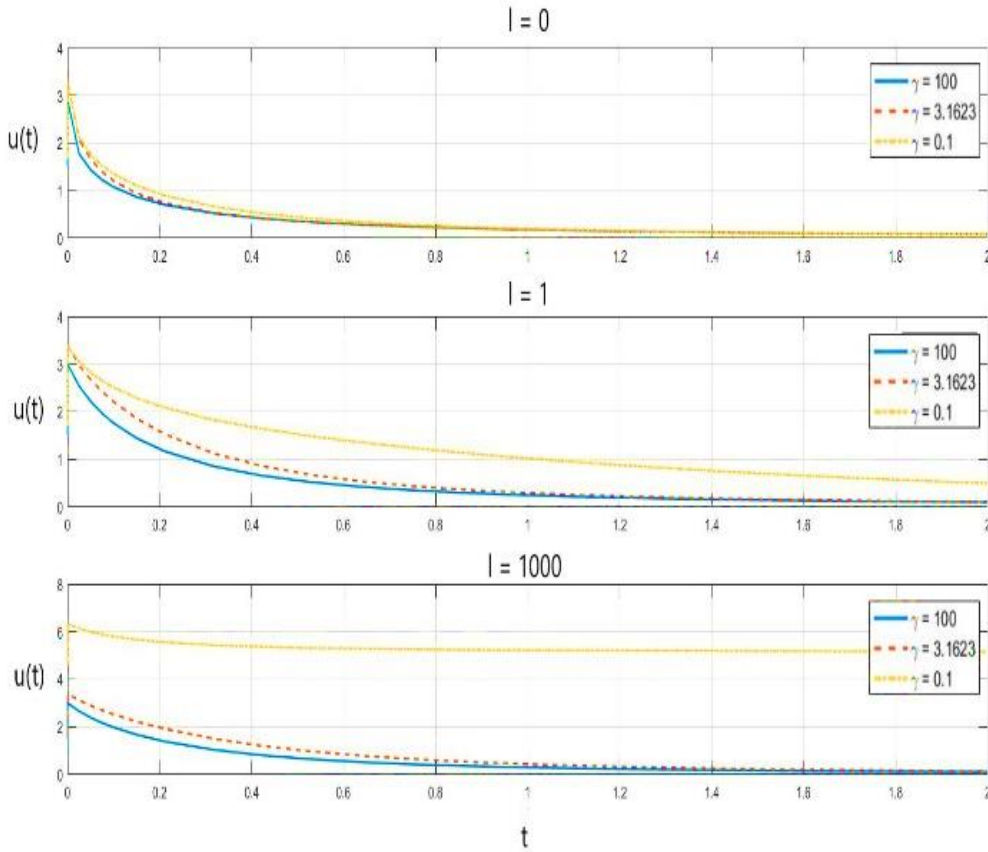
Fig. 8 Transient mobility response as function of time for no-slip, transitional and full-slip sphere with solid-to-liquid density ratio $\bar{\rho} = 1$

The findings are especially significant for the analysis of Brownian dynamics as integral of the computed response renders diffusivity according to Green-Kubo relation.

6.1 Calculation of the Mobility Response

The motion of the solid sphere is dependent on the impact due to $\mathbf{f}_\omega^{ex}$ as well as its prolonged translation within the viscous flow. As $\widehat{\bar{F}}_\omega^H$ is known, its computed value is inserted into the non-dimensional forms of equations 10 and 14 to determine the time-dependent mobility response $u(t)$. Its non-dimensional form can be expressed according to the following integral:

$$\bar{u}(t) = \frac{6\pi a \rho \, u}{\eta} = \frac{1}{2\pi} \int_{-\infty}^{\infty} \frac{e^{i\bar{\omega}\bar{t}}}{\frac{2i}{9}\bar{\rho}\bar{\omega} - \widehat{\bar{F}}_\omega^h} d\bar{\omega}$$

$$= \frac{1}{\pi} \int_0^{\infty} \mathrm{Real}\left[\frac{e^{i\bar{\omega}\bar{t}}}{\frac{2i}{9}\bar{\rho}\bar{\omega} - \widehat{\bar{F}}_\omega^h}\right] d\bar{\omega} \quad (58)$$

where $\bar{t} = \frac{\eta t}{\rho a^2}$ is the dimensionless time, and $\bar{\rho}$ stands for the solid-to-fluid density ratio.

We compute the mobility response as a function of time by numerically computing the integral in eq. 58. To ensure a fast convergence, the procedure is divided into two steps representing the slowly decaying integrant properly for $\bar{\omega} \to \infty$. Firstly, the integral is evaluated

numerically using Simpson method from the limit $\bar{\omega} = 0$ to $\bar{\omega} = 10^5$. Then, the asymptotic behavior of the integrant for the high-frequency regime is estimated by Taylor series expansion in $\frac{1}{\sqrt{(\omega)}}$ and the first two terms with $\bar{\omega}^{-1}$ and $\bar{\omega}^{-\frac{3}{2}}$ are integrated analytically from 10^5 to ∞. Both results are finally added to obtain u(t) ensuring that it is calculated with less than 0.01% relative error.

6.2 Impulse Induced Transient Translational Velocity

We present the translational velocity of the particle as a temporal function in Figs. 8 and 9 where the motion is caused by the impulsive external force acted at time $\bar{t} = 0$. For these plots, the solid-to-liquid density ratio $\bar{\rho}$ is taken as either 1 or 1000 representing colloids or aerosols, respectively. The curves are produced within a non-dimensional time range from $\bar{t} = 0$ to $\bar{t} = 2$ to ensure proper focus on short- range transiency. In both figures, we created three sub-figures with three values of $\bar{l}$ representing no-slip, partial slip, and full slip conditions. Moreover, three curves with different $\bar{\gamma}$ in each sub-figure are showing transient variations in parametric regimes corresponding to impermeable, transitional, and permeable particles, respectively. In all these simulations, we fix $\epsilon = 10^{-10}$ in order to choose the values of $\bar{\gamma}$ that can span from impermeable to permeable spheres.

We observe that the velocity of the no-slip impermeable neutrally buoyant particle is 3/2 at t = 0 and
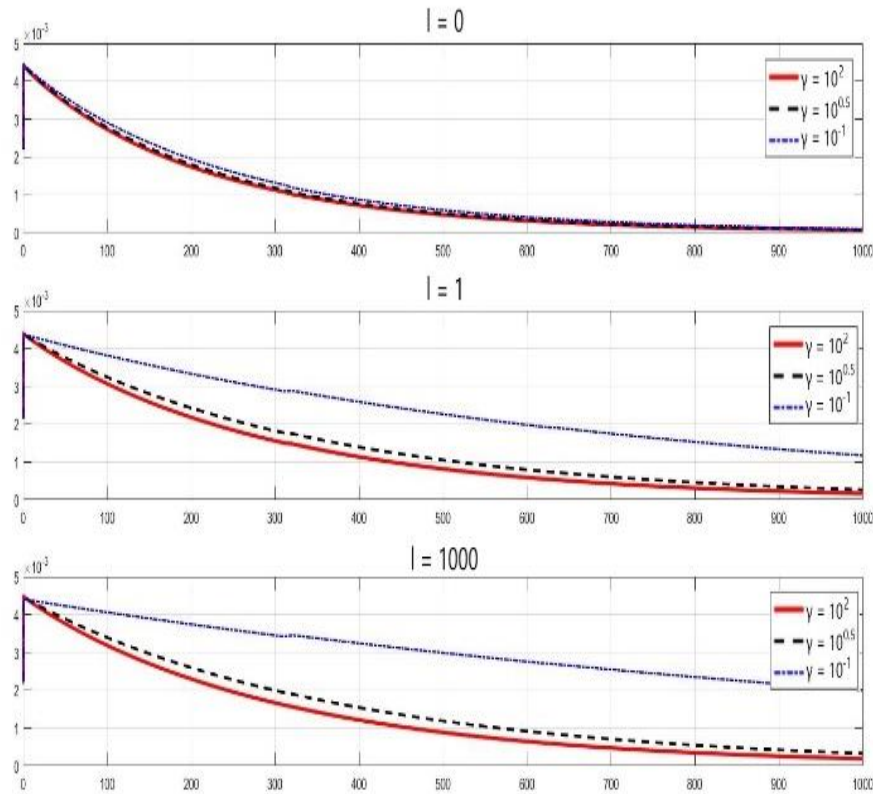
2294

Fig. 9 Transient mobility response as function of time for no-slip, transitional and full-slip sphere with solid-to-liquid density ratio $\bar{\rho} = 1000$

3 at t → 0+. This means that the velocity becomes a step function across t = 0 from 0 value at t → 0− to 3 at t → 0+ while being at the middle of the span for t exactly 0. Such behavior appears due to the obvious effect of force impulse represented by the Dirac delta function. For density-ratio 1, the non-dimensional mass for the sphere is 2/9 whereas the added contribution from the fluid is 1/9 as seen in Fig.7. Thus, the dimensionless effective mass for the entire system is 1/3 which explains the magnitude of the step function obtained as 1/(1/3) = 3. Therefore, such corroboration further validates our analysis in the inertial regime with ballistic motion.

Similar step functions appear for all other particles where the velocity jumps from 0 to a certain value across t = 0 while attaining the middle of the span when *t* is exactly 0. The amplitude of the step function is always dictated by the combination of the particulate and added mass. Accordingly, this amplitude should be $1/\left(\frac{2\bar{\rho}}{9+\overline{M_A}}\right)$ with normalized added mass $\overline{M_A} = \frac{M_A}{6\pi\rho a^3}$ being furnished in Fig.7. All our mobility plots conform to the aforementioned relation.

In all plots, some of the features are quite intuitive. For example, the larger value of slip-length causes higher mobility. This is an expected behavior because increased *l* makes the shear stress weaker at the interface. Thus, larger *l* reduces the hydrodynamic resistance by decreasing skin friction. As a result, an impulse-induced motion becomes more sustainable in these cases. Similarly, due to resistive

force, all the curves in Fig. 8 show decaying temporal behavior for the motion of the particle after impact when *t* > 0. As $\bar{t}$ increases, the velocity of the spheres decreases and saturates to 0 relatively quickly if either the solid domain is impermeable, or the interface is no-slip. However, simultaneous occurrence of porous body and slip surface makes the decay rate significantly smaller so that asymptotic approach to 0 happens at a much higher value of $\bar{t}$. As the fluid goes inside of the particle, it finds parallel routes to cross the solid object by either going through it or circumventing it. Thus, the pressure built up across the particle opposing its motion decreases as if the body is acting like a leaky piston releasing the fluid. This effect is especially crucial for large $\bar{l}$ because the built-up pressure is the main source of hydrodynamic resistance on slip-spheres in absence of skin frictions. This is the reason behind the distinction viewed in cases with simultaneous slip and permeability compared to others. The observation can also be corroborated from the findings discussed in subsection 5.5.

In Fig. 9, we reproduce the transient mobility response with exact similar parameters like Fig. 8 except the density-ratio $\bar{\rho}$ which is assumed to be 1000 here. Such large value of $\bar{\rho}$ corresponds to the solid suspension in air. The generic decaying behavior exhibited by the curves in Fig.9 are very similar to the ones in Fig.8 except for two specific distinctions. Firstly, the step function at the initial time has a smaller amplitude in Fig.9 due to more massive particle reacting more sluggishly to unit impulse. Secondly, the decay would take longer time for

larger $\bar{\rho}$ as increased particulate inertia causes slower retardation. If the velocity-response is multiplied and time $\bar{t}$ is divided by $\left(\frac{2\bar{\rho}}{9+\overline{M_A}}\right)$, the plots for the newly normalized quantities would exhibit roughly similar curves as Fig.8 if other parameters are same. This observation can be used to formulate an approximate similarity rule to characterize transient dynamics of different solids in different fluids.

7. CONCLUSION

In this paper, we analyze the unsteady translation of a porous sphere with an external surface exhibiting partial slip while transmitting through a viscous liquid. The system is defined by the density and viscosity of the fluid as well as the permeability factor, slip-length and effective viscosity for interior flow for the solid. We consider a quiescent flow-condition for the fluid far away from the particle.

The Reynolds number of the system is low, but the temporal dependence in the particulate translation is caused by the viscous dissipation. Thus, we can neglect the convective inertia, though the temporal acceleration cannot be ignored in the dynamic equation. Accordingly, linearized unsteady Navier-Stokes equation governs the velocity field outside the porous body. In contrast, unsteady Brinkman relation for fluid motion inside a permeable solid is taken as the governing field equation for the flow inside the sphere. The mathematical formulation also includes four boundary conditions in the form of regularity at the spherical center, decay at infinity and interfacial continuity of velocity as well as stress at the external surface of the particle. The expression of interfacial stress contains the slip term making the corresponding boundary condition a mixed one instead of Dirichlet kind for no-slip surfaces.

The system of equations allows a time-invariant formulation if the analysis is cast into the frequency domain by temporal Fourier transform. Accordingly, the viscous dynamics around the particle can be characterized by a frequency-dependent friction coefficient with both real and imaginary parts. These quantities are computed as functions of frequency ω for a wide range of permeability factor, slip-length and effective interior viscosity values. The friction coefficients are presented in an appropriate non-dimensional form.

The non-dimensional friction is also presented in phase diagrams at limit $\omega \to 0$ and $\omega \to \infty$. These values under low and high frequency limits match with the known results from Stokesian and ballistic regimes, respectively. Such corroborations prove the accuracy of our analysis.

Moreover, the phase diagrams exhibit an unexpected behavior where a diminished impact of slip-length is seen when $\sqrt{\epsilon}\bar{\gamma} \gg 1$. Scaling arguments from a novel boundary-layer theory explains this coupled parametric variation adequately by identifying the correct scales for the tangential relative velocity at the interface.

The evaluated friction is used in the equation of motion for the particle to determine its time-dependent velocity response to a unit impulse. Such transient mobility exhibits the expected decaying characteristics with time. More porous particles are seen to be more mobile, as they face less opposing pressure difference across the leading and trailing points due to the leakage. Increased slip-length, in contrast, enhances mobility due to the reduction in tangential shear stress.

The mobility response is plotted for two cases with solid-to-liquid density-ratio 1 and 1000 representing suspensions in liquid as well as aerosols is air. The results from two totally different systems can be approximately collapsed into a single curve if the non-dimensional velocity and time are multiplied and divided by a factor $\left(\frac{2\bar{\rho}}{9+\overline{M_A}}\right)$, respectively. The dimension-less added mass for the velocity of the liquid domain is also presented for different values of system-defining parameters.

In general, it is seen that the friction and mobility vary considerably with permeability and slip-length. Their non-dimensional versions $\bar{\gamma}$ and $\bar{l}$ can have interesting ranges of values when the size of the particle is around 100-nm. In that range, the variation in particulate mobility is significant. Accordingly, one can conclude that nano-particle dynamics can be substantially affected by the presence of porosity and slip. Thus, the analysis presented in this article can find additional relevance if unexplained variability is encountered in phenomena involving nano-particles. For example, this can be a key consideration to understand heat conduction in nano-fluids. Similarly, the same theory may be able to explain different dynamics of apparently similar looking air-borne viruses. Our future works will be devoted to expand the scope of this work in these aforementioned applications.

ACKNOWLEDGEMENTS

CONFLICT OF INTEREST

There is no conflict of interest for any of the authors.

AUTHORS CONTRIBUTION

P. Cano Fossi did mathematical analysis, numerical coding and data analysis. **P. Nourian** helped in the analysis and coding. **R. Khare** participated in the problem identification and manuscript preparation and S Bhattacharya worked on all these activities.

REFERENCES

Chen, G. (2001). Ballistic-diffusive heat-conduction equations. *Physical Review Letters 86*, 2297–2300. https://doi.org/10.1103/PhysRevLett.86.2297

Dixon, A. G., Taskin, M. E., Nijemeisland, M., & Stitt, E. H. (2010). CFD method to couple three-dimensional

transport and reaction inside catalyst particles to the fixed bed flow field. *Industrial and Engineering Chemistry Research, 49* (19), 9012–9025. https://doi.org/10.1021/ie100298q

Eastman, J. A., Choi, S. U. S., Li, S., Yu, W., & Thompson, L. J. (2001). Anomalously increased effective thermal conductivities of ethylene glycol-based nanofluids containing copper nanoparticles. *Applied Physics Letters* 78, 718–20. https://doi.org/10.1063/1.1341218

Fahy, J. V., & Dickey, B. F. (2010). Airway mucus function and dysfunction. *New England Journal of Medicine*, *363* (23), 2233–2247. https://doi.org/10.1056/nejmra0910061

Furst, E. M., & Squires, T. M. (2017). *Microrheology*. Oxford University Press.

Higdon, J., & Kojima, M. (1981). On the calculation of Stokes' flow past porous particles. *International Journal of Multiphase Flow*, *7*(6), 719–727. https://doi.org/10.1016/0301-9322(81)90041-0

Huang, H. Y., & Keh, H. J. (2015). Diffusiophoresis in suspensions of charged porous particles. *Journal of Physical Chemistry B, 119*(5), 2040–2050. https://doi.org/10.3390/colloids4030030

Karim, M., Kohale, S. C., Indei, T., Schieber, J. D. & Khare, R. (2012). Determination of viscoelastic properties by analysis of probe-particle motion in molecular simulations. *Physical Review E, 86* (5), 051501. https://doi.org/10.1103/PhysRevE.86.051501

Karim, M., Indei, T., Schieber, J. D., & Khare, R. (2016) Determination of linear viscoelastic properties of an entangled polymer melt by probe rheology simulations. *Physical Review E, 93*(1), 012501. https://doi.org/10.1103/PhysRevE.93.012501

Keh, H. J., & Chou, J. (2004) Creeping motions of a composite sphere in a concentric spherical cavity. *Chemical Engineering Science*, *59*(2), 407–415. https://doi.org/10.1016/j.ces.2003.10.006.

Keh, H., & Lu, Y. (2005). Creeping motions of a porous spherical shell in a concentric spherical cavity. *Journal of Fluids and Structures*, *20*(5), 735–747. https://doi.org/10.1016/J.JFLUIDSTRUCTS.2005.03.005

Kincaid, J. M., & Cohen, E. G. D. (2002). Nano- and pico-scale transport phenomena in fluids. *Journal of Statistical Physics, 109*, 361–71. https://ui.adsabs.harvard.edu/link_gateway/2002JSP...109..361K/doi:10.1023/A:1020433725023

Looker, J. R., & Carnie, S. L. (2004). The hydrodynamics of an oscillating porous sphere. *Physics of Fluids, 16*(1), 62–72. https://ui.adsabs.harvard.edu/link_gateway/2004PhFl...16...62L/doi:10.1063/1.1630051

Marconnet, A. M., Panzer, M. A., & Goodson, K. E. (2013). Thermal conduction phenomena in carbon nanotubes and related nanostructured materials.

Reviews of Modern Physics, 85,1295–1326. https://doi.org/10.1103/RevModPhys.85.1295

Masliyah, J. H., Neale, G., Malysa, K., Theodorus, G. M. & V. D. Ven (1987). Creeping flow over a composite sphere: solid core with porous shell. *Chemical Engineering Science, 42*(2), 245–253. https://doi.org/10.1016/0009-2509(87)85054-6

Mason, T. G. (2000). Estimating the viscoelastic moduli of complex fluids using the generalized Stokes–Einstein equation. *Rheologica Acta, 39*(4), 371–378. https://doi.org/10.1007/s003970000094

Mason, T. G., & Weitz, D. A. (1995). Optical measurements of frequency-dependent linear viscoelastic moduli of complex fluids. *Physical Review Letters, 74*(7), 1250–1253. https://doi.org/10.1103/physrevlett.74.1250

Mundargi, R. C., M. G. Potroz, S. Park, H. Shirahama, J. H. Lee, J. Seo, & N. J. Cho (2016). Natural sunflower pollen as a drug delivery vehicle. *Small*, *12*(9), 1167–1173. https://doi.org/10.1002/smll.201500860

Navardi, S., & Bhattacharya, S. (2013) General methodology to evaluate two-particle hydrodynamic friction inside cylinder-bound viscous fluid. *Computers and Fluids*, *76*,149–169. https://doi.org/10.1016/j.compfluid.2013.01.004

Navardi, S., Bhattacharya, S., & Wu, H. (2015) Stokesian simulation of two unequal spheres in a pressure-driven flow through a cylinder. *Computers and Fluids*, *121*, 145–163. http://dx.doi.org/10.1016/j.compfluid.2015.07.027

Neale, G., Epstein, N., & Nader, W. (1973). Creeping flow relative to permeable spheres. *Chemical Engineering Science, 28*(10), 1865–1874. https://ui.adsabs.harvard.edu/link_gateway/1973ChEnS..28.1865N/doi:10.1016/0009-2509(73)85070-5

Nourian, P., Islam, R., & Khare, R. (2021). Implementation of active probe rheology simulation technique for determining the viscoelastic moduli of soft matter. *Journal of Rheology*, *65*(4), 617–632. https://doi.org/10.1122/8.0000071

Prakash, J., & Raja Sekhar, G. (2012). Arbitrary oscillatory Stokes flow past a porous sphere using Brinkman model. *Meccanica*, *47*(5), 1079–1095. http://dx.doi.org/10.1007/s11012-011-9494-1

Prakash, J., & Sekhar, G. (2017). Slow motion of a porous spherical particle with a rigid core in a spherical fluid cavity. *Meccanica*, *52*(1), 91–105. http://dx.doi.org/10.1007/s11012-016-0391-5

Premlata, A. R., & Wei, H. H. (2019). The basset problem with dynamic slip: slip-induced memory effect and slip-stick transition. *Journal of Fluid Mechanics, 866*, 431–449. http://dx.doi.org/10.1017/jfm.2019.57

Schuster, B. S., Suk, J. S., Woodworth, G. F., J. Hanes (2013). Nanoparticle diffusion in respiratory mucus from humans without lung disease. *Biomaterials*, *34*(13), 3439–46. https://doi.org/10.1016/j.biomaterials.2013.01.064

Solsvik, J., & Jakobsen, H. A. (2011). Modeling of multicomponent mass diffusion in porous spherical pellets: Application to steam methane reforming and methanol synthesis. *Chemical Engineering Science, 66*(9), 1986–2000. http://dx.doi.org/10.1016/j.ces.2011.01.060

Tsai, S. C., & Lee, E. (2019). Diffusiophoresis of a highly charged porous particle induced by diffusion potential. *Langmuir*, *35*(8), 3143–3155. https://doi.org/10.1021/acs.langmuir.8b04146

Vahedi, A., & Gorczyca, B. (2012). Predicting the settling velocity of flocs formed in water treatment using multiple fractal dimensions. *Water Res*, *46*(13), 4188–94. https://doi.org/10.1016/j.watres.2012.04.031

Vainshtein, P., & Shapiro, M. (2009). Forces on a porous particle in an oscillating flow. *Journal of Colloid and Interface Science*, *330*(1), 149–155. http://dx.doi.org/10.1016/j.jcis.2008.10.050

Wei, Y. K., & Keh, H. J. (2004). Diffusiophoretic mobility of charged porous spheres in electrolyte gradients. *Journal of Colloid and Interface Science*, *269*(1), 240–250. https://doi.org/10.1016/j.jcis.2003.08.054

Yao, X., Ng, C. H., Teo, J. R. A., Marcos, & Wong, T. N. (2019). Slow viscous flow of two porous spherical particles translating along the axis of a cylinder. *Journal of Fluid Mechanics*, *861*, 643-678. https://doi.org/10.1017/jfm.2018.918

Yu, Q., & Kaloni, P. (1988). A Cartesian-tensor solution of the Brinkman equation. *Journal of engineering mathematics*, *22*(2), 177–188. https://doi.org/10.1007/BF02383599